CORRESPONDENCE



Spot melting improves the morphology of ultrathin wall builds:

a numerical study

- Boris Korneev¹ · Sergei Belousov¹ · Maria Bogdanova¹ · Inna Iskandarova² · Anastasia Perepelkina^{2,3} ·
- 5 Andrey Zakirov² · Boris Potapkin²
- 6 Received: 31 May 2025 / Accepted: 28 September 2025
- © The Author(s), under exclusive licence to Springer Nature Switzerland AG 2025

8 **Abstract**

Additive manufacturing of thin structures by powder bed fusion (PBF) presents challenges related to melt pool instability and thermal stress accumulation, which often lead to morphological defects and print failures. In this work, we investigate the influence of different scan strategies—continuous scanning in fixed and alternating directions, and spot melting—on the 12 morphology and stability of single-track-thick walls using high-fidelity, three-dimensional mesoscopic simulations of the 13 electron beam PBF (PBF-EB) process. The simulations describe melt pool dynamics and heat transfer with a micron resolution using a thermal lattice Boltzmann method coupled with additional physical models and methods required for the mul-15 tilayer PBF-EB simulation. Our results show that during spot melting, the hydrodynamic instabilities are suppressed, which 16 enables the formation of defect-free ultrathin walls. This effect is explained by the observed differences in melt pool dynamics AQ2 17 between continuous and spot melting strategies. These findings demonstrate the potential of spot melting for high-resolution

metal additive manufacturing and provide insights into simulation and experimental techniques for spot melting in PBF.

23

24

25

26

27

28

29

30

31

32

33

34

35

36

37

38

40

41

42

43

44

45

46

19 1 Introduction

- 20 Powder bed fusion (PBF) is a manufacturing method capable
- 21 of producing parts with complex geometries. Lightweight
- 22 structures, such as thin walls, lattices, and bio-inspired

Α1

korneev@hipercone.com A2

Sergei Belousov АЗ

belousov@hipercone.com A4

Maria Bogdanova Α5

bogdanova@hipercone.com

Inna Iskandarova A7

A6

inna@kintech.ru Α8

Anastasia Perepelkina Α9 A10 aperepelkina@kintech.ru

Andrey Zakirov A11

zakirov@kintech.ru A12

Boris Potapkin A13

potapkin@kintech.ru A14

Hipercone Limited, Jerusalem, Israel A15

Kintech Lab (Russia), Moscow, Russian Federation A16

Keldysh Institute of Applied Mathematics, Moscow, A17 Russian Federation A18

designs, are of particular interest due to their potential applications in aerospace, biomedical, and energy sectors [1-3]. Single-track thickness or ultrathin walls are attractive in terms of achieving high weight-to-surface area ratio [4, 5]. However, experimental studies report a lower limit on wall thickness [6, 7] below which the production of stable, continuous structures becomes challenging.

The limitations arise from several factors. The primary cause is melt pool instability [8]. During continuous scanning, the melt pool tends to elongate and becomes susceptible to hydrodynamic effects, such as Marangoni-driven flow and Plateau-Rayleigh instability. These phenomena can result in non-uniform material fusion and morphological defects. Another reported cause of melt pool instability [9] is melt overheating, which leads to excessive evaporation and recoil pressure, further destabilizing the melt pool. A separate issue relates to thermomechanical effects. Uneven heat input during the thin-wall build can induce wall distortion and cracking [10].

A possible approach to mitigate these effects is the use of more complex scan strategies, as opposed to a single continuous line scan at each layer. In the spot melting scan strategy, energy input is applied as a sequence of short duration, spatially separated beam pulses [11]. The study by [12] reports that this approach helps to localize the melt region,



Journal: Large 40964 Article No: 1377 Pages: 9 MS Code: 1377 Dispatch: 3-10-2025

98

99

100

101

102

103

104

105

106

107

108

109

110

111

112

113

114

115

116

117

118

119

120

121

122

123

124

125

126

127

128

129

130

131

132

133

134

135

136

137

138

139

140

142

143

144

145

reduce convective transport, and distribute heat more uniformly across the layer. In [9], an alternative approach was employed, where, in each layer, a single line was repeated several times with a correspondingly increased scanning velocity, also helping to suppress melt pool dynamics instabilities.

In this work, we consider the electron beam powder bed fusion (PBF-EB) process employing a spot melting approach for the fabrication of ultrathin walls with a thickness in the range of 200-250 µm, which is below reported limiting thickness [6, 7]. Inconel 625, a nickel-based superalloy widely used in additive manufacturing, is selected as the material for this investigation. To focus on the underlying physical phenomena, three-dimensional mesoscopic simulations of PBF-EB process are performed, resolving melt pool dynamics and heat transfer at the powder particle scale [13, 14]. Three scan strategies are simulated: continuous scanning in fixed and alternating directions, and spot melting. The results are analyzed in terms of differences in the melt pool dynamics, temperature history, and resulting wallheight profile across multiple layers.

2 Methods

48

49

50

51

52

53

54

55

56

57

58

59

60

61

62

63

65

66

67

68

70

71

72

73

74

75

76

77

78

79

80

81

82

83

84

85 86

87

88

89

90

91

92

93

94

95

2.1 PBF-EB numerical model

The additive manufacturing process is modeled at a melt pool level using the KiSSAM [15] simulation package, which includes models for the powder bed fusion and powder deposition processes.

A free surface thermal lattice Boltzmann method (LBM) [16] is a core method of KiSSAM. This method solves the governing equations of fluid dynamics and heat transfer on a uniform Cartesian mesh (melt pool grid) using the D3Q27 lattice model, with the liquid interface tracked via a volume-of-fluid approach.

A dynamic mesh is used, updated accordingly to focus computational resources on the region surrounding the molten material. Thermal transport as well as fluid dynamics is modeled with the thermal LBM in the vicinity of the melt (melt pool grid). On a coarser grid that extends beyond it, the heat equation is solved using the finite-difference scheme. This configuration maintains high accuracy in capturing the fluid dynamics while allowing temperature evolution to be solved over a larger scale domain.

Pressure boundary conditions are applied at the liquidfree surface, and adiabatic boundary conditions are imposed for the heat equation.

Additional physical phenomena proven to play a significant role in the powder bed fusion process are taken into account [17]. Surface tension and wetting phenomena are approximated using a template-sphere model [16] extended to three dimensions. The simulation includes models for Marangoni convection [18], radiation cooling, and drag in the mushy zone [19]. Evaporation is also taken into account by estimating the corresponding mass and energy losses and calculating the recoil pressure acting on the surface [20, 21]. For electron propagation, a ray tracing method is used with the Monte Carlo model of electron scattering [22, 23].

Powder spreading is modeled using PowDEM, a discrete element (DEM) module [24] bundled with KiSSAM. Spherical mono- and polydisperse powders are considered. Gravity-fed and recoater-fed recoating can be simulated. The recoater interaction with the built part is neglected as it appears to be important for thin walls with the thickness less than 100 µm, as shown in [25].

KiSSAM and PowDEM are written on CUDA C++ and they run on NVIDIA graphics processing units (GPUs). Further technical details of the implemented models, numerical schemes and algorithms are published in the article describing the KiSSAM framework [26] and in the software documentation (http://www.kissam.cloud/physical [15]).

2.1.1 Multilayer simulation

The simulation of several layers of corresponding part fabrication is carried out in the following stages.

The process begins with the deposition of powder onto a substrate of a given shape, which is simulated in PowDEM. Subsequently, the preheating and melting phases are distinguished. The preheating phase and the sintering of the powder are not simulated directly; instead, a uniform initial temperature corresponding to the preheating temperature is assigned to the numerical domain at the start of each layer and solid powder particles remain immobile during the melting phase, as implied by prior sintering. The melting and solidification dynamics, fluid flow, and heat transfer are modeled in KiSSAM as described in Sect. 2.1.

Once the melt has fully solidified, the resulting solid fraction field is processed to extract a surface representation. The resulting mesh then serves as the substrate for the next powder layer.

This cycle of powder spreading, melting, solidification, and surface extraction is repeated to simulate the desired number of layers.

2.2 Material parameters

Simulations are carried out for the Inconel 625 alloy. The thermophysical properties used in the numerical model are summarized in Table 1 in the Appendix. These parameters AQ3 1 have been extensively validated in the prior works [8, 27]. With this parameters set, the model has shown good agreement with the experimental results for single-track geometries, including track depth and width, as well as for key



Journal : Large 40964 Article No: 1377 Pages: 9 MS Code: 1377 Dispatch: 3-10-2025

melting regimes, such as balling and keyholing [27]. Furthermore, the same material description has demonstrated predictive capability for the formation and morphology of thin-walled structures fabricated by laser-based PBF [8].

3 Problem statement

In this study, Inconel 625 material is used for the substrate and the powder with a particle size range of 45–105 μ m. The constant preheating temperature $T_{\rm preheat} = 1000~{\rm K}$ is assumed to be the initial condition before the start of each layer scan.

An electron beam is used with a power of P=270 W, corresponding to a voltage of U=60 kV and a current of I=4.5 mA. The Gaussian beam is considered having a spot size of $D_{4\sigma}=250$ μ m. Such spot size is selected to simulate thin walls with a target thickness of approximately 200-250 μ m.

The printed structures are ultrathin walls, built with a single track per layer. Each track length is $L_{\rm scan}=5$ mm, and the platform step between layers is 50 μ m. 25 layers are simulated.

Three scanning strategies are examined: (i) continuous scan with the same scan direction in each layer (FF), (ii) continuous scan with alternating scan direction in each layer (BF), and (iii) spot melting scan with the same spot sequence in each layer (SM). Figure 1 explains differences between FF and BF scan strategies.

The following beam scanning speed is used for BF and FF scan strategies: S = 0.6 m/s. Scanning time at each layer $t_{\rm scan} = L_{\rm scan}/S \approx 8.33$ ms. In case of the SM scan strategy, same total scanning time $t_{\rm scan}$ is kept at each layer.

For the SM scan strategy, the following jumping spot sequence is selected, in which scheme is shown in Fig. 2. The distance between the nearest spots is $d_s = 100 \, \mu \text{m}$ resulting in overall number of spots $N_{\text{spots}} = \left[L_{\text{scan}} / d_s \right] = 51$. An exposure time for each spot is $t_{\text{exp}} = t_{\text{scan}} / N_{\text{spots}} \approx 163.4 \, \mu \text{s}$. The jump distance is $d_j = 500 \, \mu \text{m}$. The jump duration between the next spots is assumed to be negligibly short. Figure 3 illustrates the beam scan path in the x-t diagram, where x represents the scanning direction and t denotes the time elapsed during the layer-wise scan.

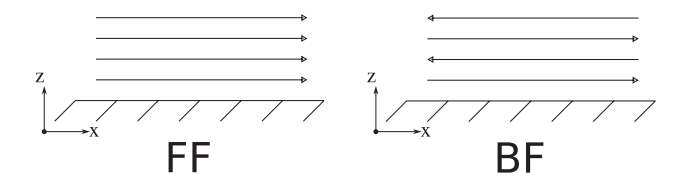


Fig. 1 FF and BF scan patterns

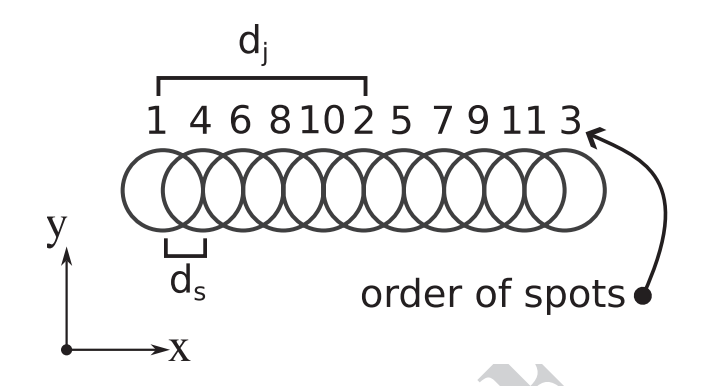


Fig. 2 Scheme of spot sequence explained on a short track example

3.1 Numerical parameters and domain

The lattice size in the melt pool grid is 4 μ m is used; the time step is 50 ns. The total domain size is 7 mm \times 2 mm \times 4 mm. The substrate thickness is 2 mm. Cartezian coordinate system will be used in the following sections, with the origin corresponding to the start of the wall scan at the first layer and x axis associated with the scanning direction. It is illustrated in Fig. 4.

3.2 Computational resources

All simulations were carried out on a computer equipped with 8 NVIDIA RTX 3090 graphics processing units, each featuring 24 GB of onboard memory. The single multilayer simulation was run on a single GPU. Typical time of simulation of one layer is 5 h. Full set of simulations (3 × 25 layers) lasted about a week using 3 GPUs.

4 Results 201

4.1 Melt pool dynamics and layer-wise melt pool stability

In Fig. 5, the melt pool is captured for different layers of the build at the same time moment from the corresponding layer scan beginning. The time moment is chosen when the melt pool is well developed. Shades of orange represent the liquid in Fig. 5.

Starting from the very first layer, the melt pool formed during the FF and BF scans exhibits a typical elongated shape aligned with the scan direction. In contrast, during the SM scan, the melt pool consists of several short melt spots. At higher layers, these individual melted spots begin to merge; however, this merging does not significantly destabilize the overall melt pool.

For the FF case, the beam path is identical at each layer, so is the melt pool flow direction, which is known to be



220

221

222

223

224

225

226

227

228

229

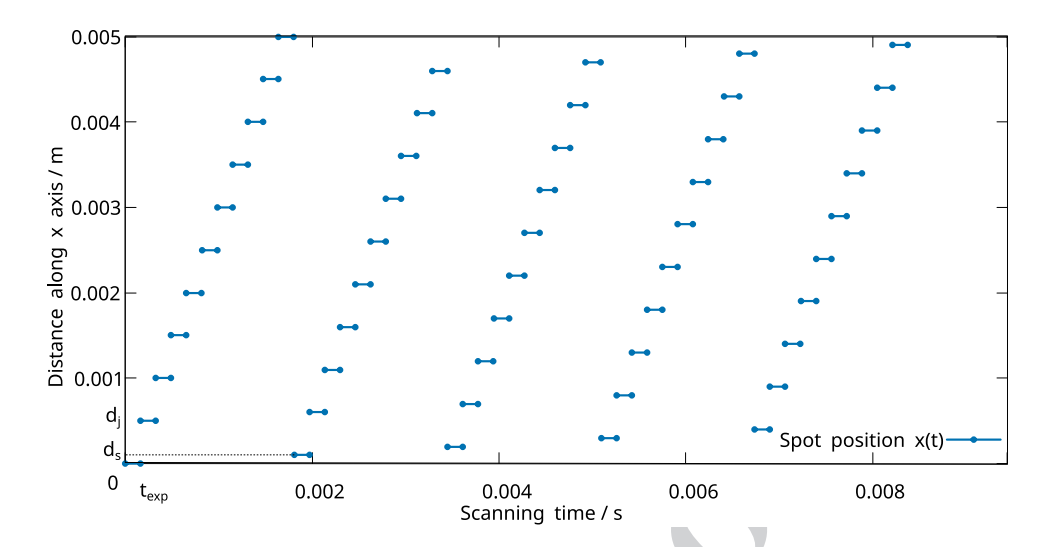
230

231

232

233

Fig. 3 *x*–*t* diagram of beam scan path in case of spot melting



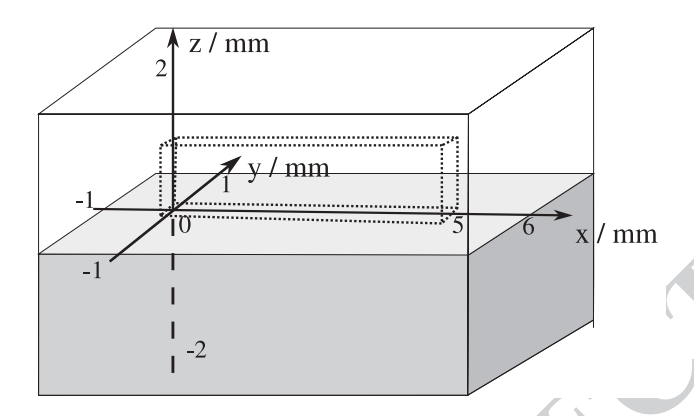


Fig. 4 Schematic of the simulation domain. The wall is represented by dotted lines

mainly opposite to the beam path. This leads to a higher wall height at the beginning of the scan (see Figs. 5 and 6) and a lack-of-fusion pores formation closer to the end of the scan (Fig. 6).

For the BF case, no asymmetry is observed for the wall profile at the edges compared to the FF scan. This is because of the change in the scan direction at every layer. However, the longer melt pool is still prone to hydrodynamic instabilities, in particular the Plateau–Rayleigh instability. Melt pool breakup can be seen for the BF case in Fig. 5. Once formed in the central region of the wall, the wall profile perturbation turns into a defect, as shown in Fig. 6 for the BF scan.

Finally, for the SM case, the spot melting scan strategy helps solve both problems. The melt is split into several short melt regions, which significantly reduces mass transfer and benefits in overall melt stability.

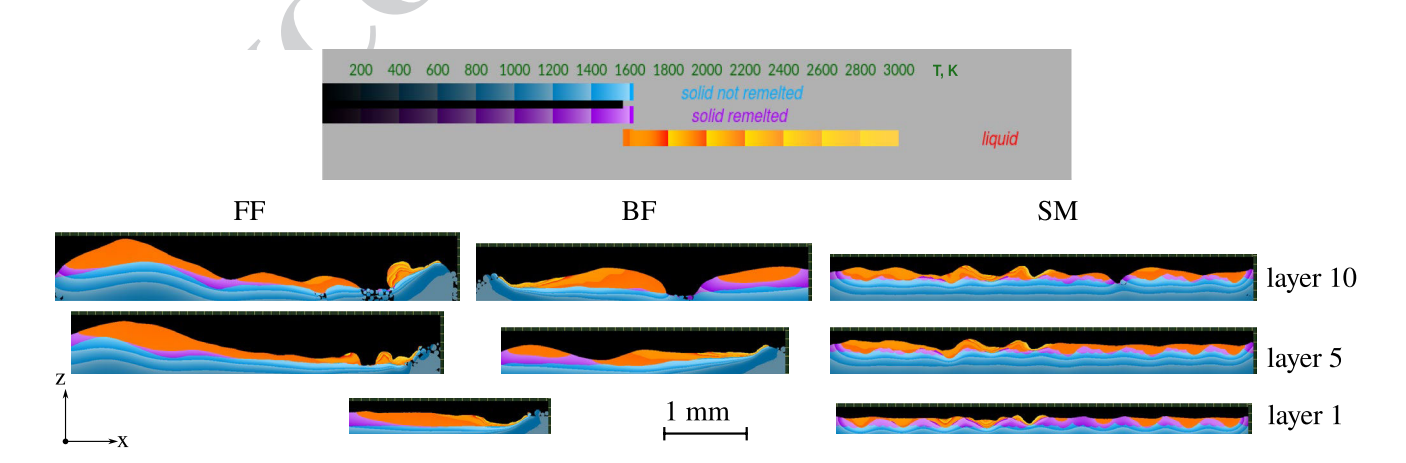


Fig. 5 Melt pool at time moment $t = 7.5 \times 10^{-3}$ s from the scan start at the corresponding layer—1 (bottom), 5 (middle), and 10 (top). Left column: FF scan, center: BF scan (FF and BF are identical for the first layer), right: SM scan



	Journal : Large 40964	Article No: 1377	Pages: 9	MS Code: 1377	Dispatch : 3-10-2025
--	-----------------------	------------------	----------	---------------	----------------------

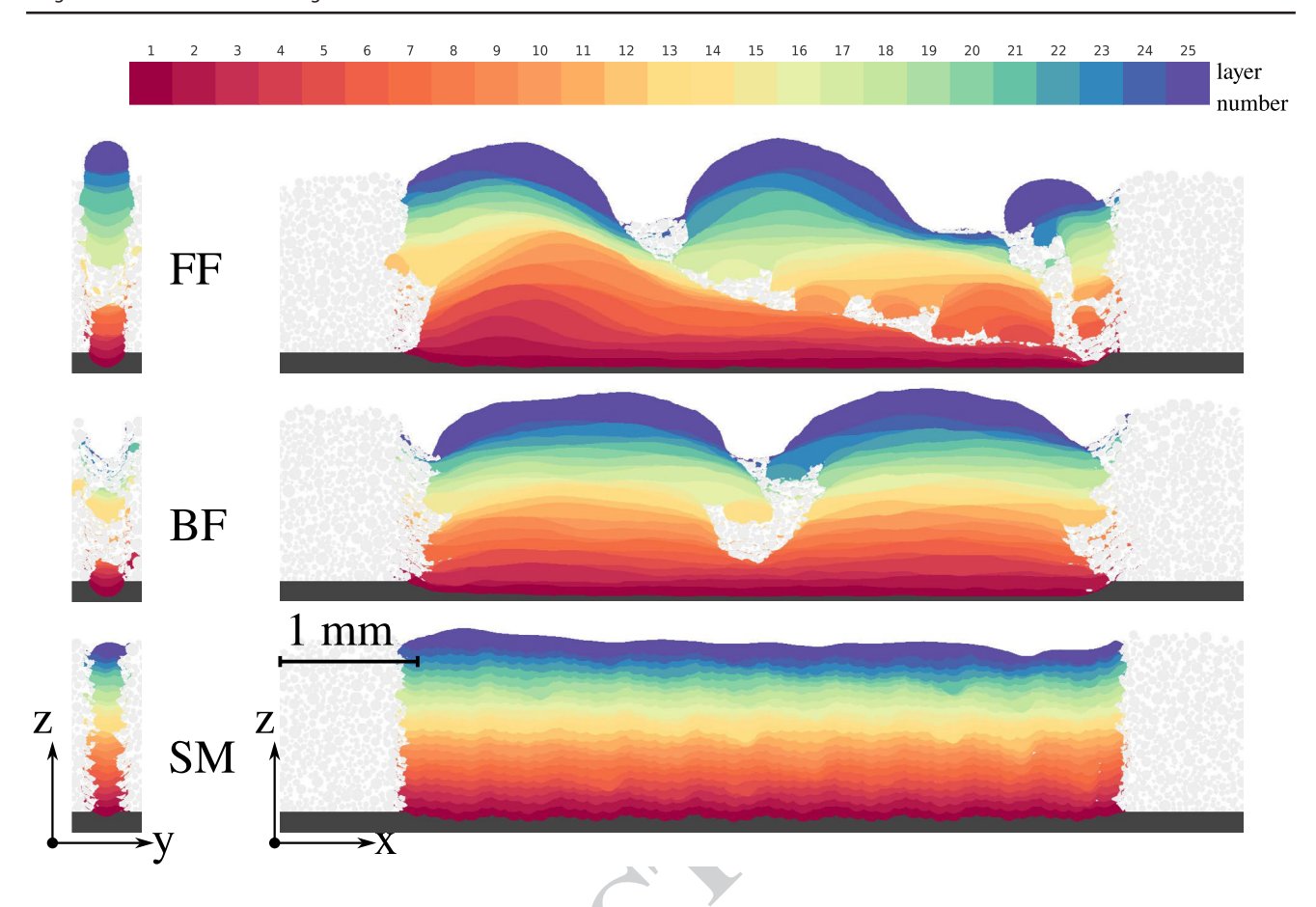


Fig. 6 Top: FF scan, middle: BF scan, and bottom: SM scan. Left: cross-section; right: longitudinal section through the middle of the wall (25 layers) is shown. Color indicates the material fused to the thin wall in the corresponding layer. Substrate is dark gray; powder is light gray

4.2 Temperature history

To examine the temperature history, a set of 25 temperature probes was introduced, placed in the following positions in the numerical domain, described by the following formula (1):

$$P_i = (2.5, 0.0, -0.1 + 0.05i) \text{ mm}, i = \overline{1, 25}.$$
 (1)

First, let us examine the first layer of the build in detail. In Fig. 7, we study the time evolution of the temperature captured in the point P_1 . Figure 8 shows the temperature distribution in space along the line parallel to the x axis drawn through the point P_1 at a specified time moment $t = 7.5 \times 10^{-3}$ s from the start of the scan, when the scanning is close to the end of the track for the FF strategy.

As expected, Figs. 7 and 8 demonstrate that the heat is distributed more uniformly along the track during the SM scan. Note that for the same probe position, the temperature does not exceed the liquidus temperature $T_{\rm liquidus}$ for the SM case.

Qualitatively, similar behavior is observed across successive layers of the wall, as shown in Fig. 9. However, the temperature histories recorded at different layers by the corresponding probes do not coincide exactly. For example, the absence of peaks above the melting point in the FF scans for layers 5 and 9 and the notable difference in the temperature curve for SM layer 17 stand out. This can be explained by the uniform probe positioning, where the first probe is placed $50~\mu$ deep in the substrate at Layer 1, and each subsequent probe is raised by a constant platform step of $50~\mu$ per layer [see Eq. (1)]. However, variations in the wall-height profile and temperature distribution between layers, particularly in the less stable FF case, result in these observed differences.

5 Discussion

In the present work, irregularities in the wall-height profile are attributed to surface tension and wetting forces, which can trigger melt pool instabilities of the Plateau–Rayleigh type. This mechanism was first proposed in [8] for the



Fig. 7 Temperature history for SM and continuous (FF) scan. First layer is shown; temperature probe P_1 is used (see Eq. (1))

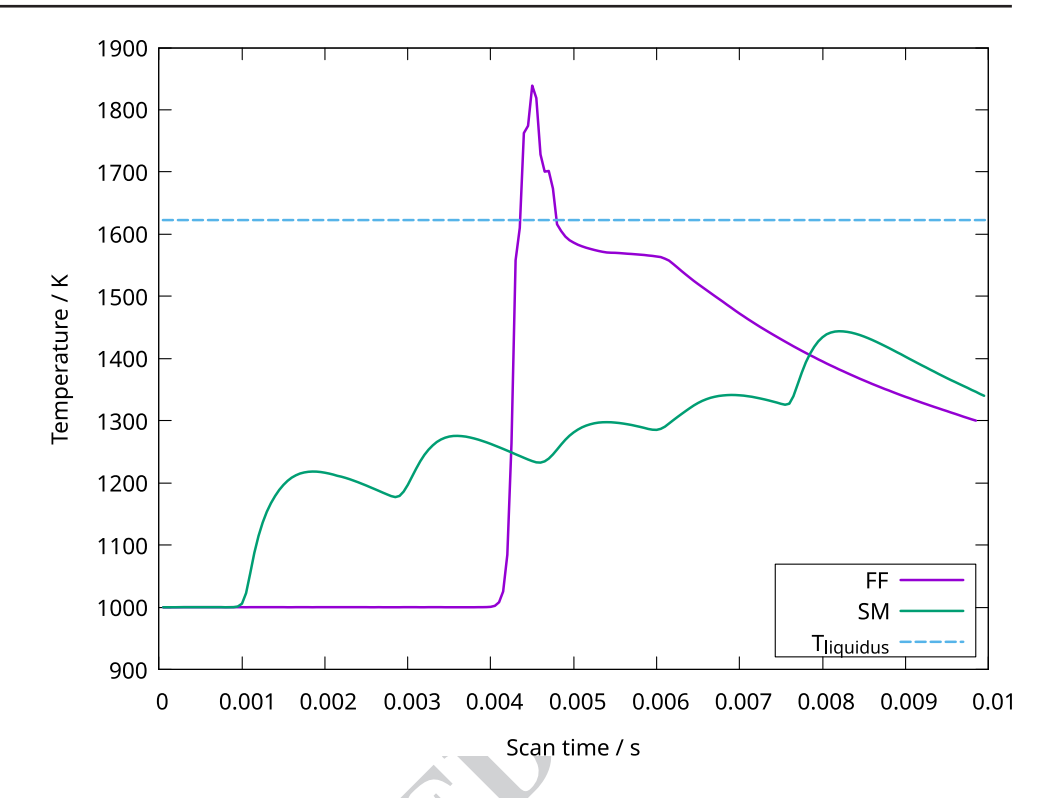
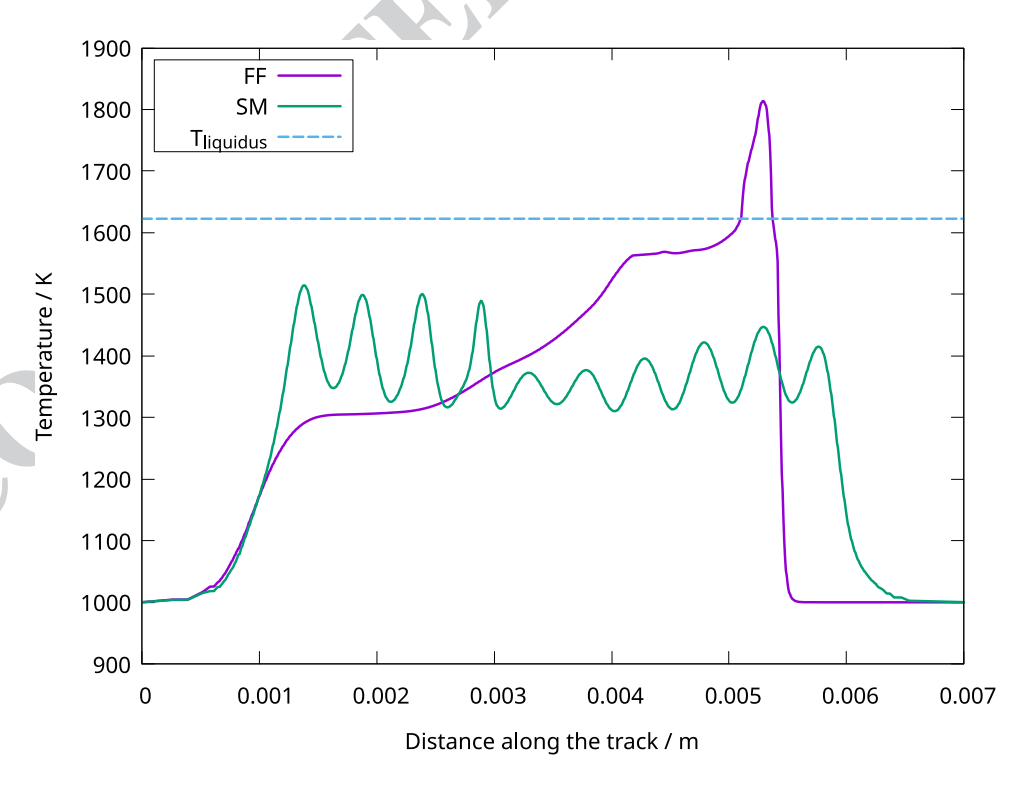


Fig. 8 Temperature distribution along the track under the laser scan path at a depth of 50μ in the substrate. Time moment $t = 7.5 \times 10^{-3}$ s; first layer of the build is shown



PBF-L process, where the wall thickness was $100-150 \,\mu m$ and the number of layers was 10. The results obtained in the present study for the FF case are qualitatively consistent with those simulated in [8] and experimentally confirmed in [28], both showing a pronounced elevation at the beginning of the

wall (where the laser scan is initiated in each layer) and a lack-of-fusion region at the end of the wall. These similarities indicate that, despite differences in process parameters and scale, certain instability mechanisms remain relevant across multiple PBF conditions.

277

278

279

280

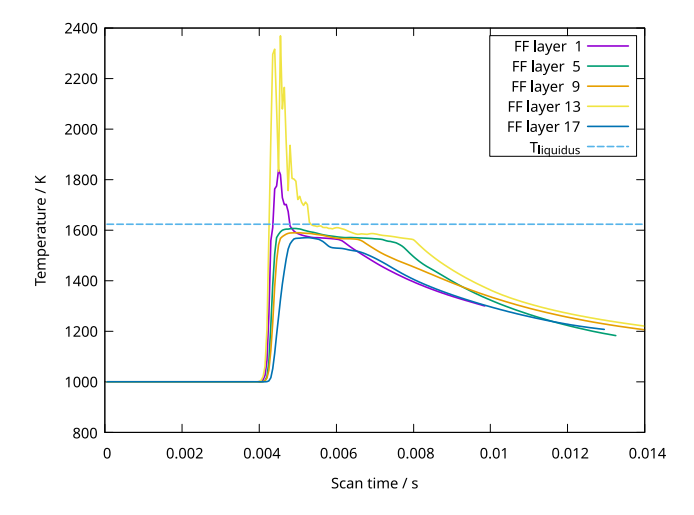
281

272

273

274

275



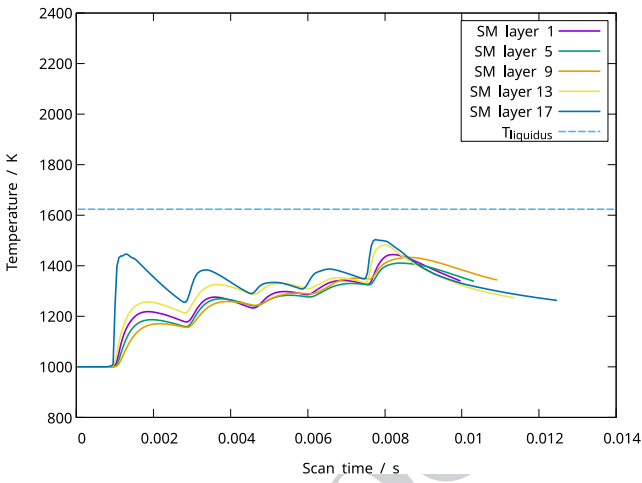


Fig. 9 Layerwise temperature history for FF case (left) and SM case (right). For the *i*-th layer, a probe P_i is used with the probe coordinates defined by the Eq. (1)

Semjatov, Wahlmann, and Körner [9] proposed a different primary mechanism for thin-wall instability and surface roughness, namely melt overheating, leading to excessive evaporation and recoil pressure that destabilize the melt pool. There are two key differences in the problem statement between Semiatov et al. [9] and the present study: (i) the target wall thickness is 200-250 um in our work versus approximately 1 mm in Semjatov et al., and (ii) the number of layers is 25 in our case versus several hundred in theirs. The profile roughness reported by Semjatov et al. reached up to 200 µm for the continuous single line builds. These distinctions suggest that the relative importance of different instability mechanisms may depend strongly on the geometric scale of the build, highlighting the need for a dedicated parametric study as a promising topic for future research. Beyond that, the instabilities observed during the first few layers in our simulations may diminish as the build height increases. Investigating how these early stage instabilities evolve over hundreds of layers is an additional interesting direction for future work.

Both the present work and Semjatov et al. report a progressive reduction in melt pool instability when implementing a complex scan strategy, although the underlying explanations differ. In our interpretation, spot melting stabilizes the melt pool by effectively dividing it into smaller, more stable ones. Semjatov et al. attributed the improved geometry in their multiple-interaction approach primarily to reduced evaporation resulting from lower melt overheating. While this represents a different mechanism, it is nevertheless complementary to our findings. The relative contribution of each mechanism likely depends on the specific processing conditions, and clarifying this dependence remains an important direction for future research.

6 Conclusion

Three thin-wall structures were simulated at the mesoscale using the KiSSAM software. Powder spreading was modeled via the discrete element method (DEM), whereas the melting stage was resolved using a D3Q27 free-surface thermal lattice Boltzmann method. All simulations were performed under identical parameters, differing solely in the scan strategy: two employed continuous scanning and one utilized a spot melting approach.

The results indicate that wall morphology is highly sensitive to the scan strategy employed. In this specific setup, the spot melting approach yielded more uniform wall geometry and smoother surface profiles compared to continuous scanning.

This difference is attributed to melt pool dynamics. Unlike continuous scanning, which generates a longer, less stable melt pool prone to hydrodynamic instabilities, spot melting creates a sequence of shorter, more stable melt pools, contributing to improved geometric uniformity and reduced surface irregularities.

Additionally, spot melting leads to a more even energy distribution along the scan path, resulting in a more uniform wall heating, which could lead to different thermomechanical characteristics of thin walls built by continuous line melting and spot melting.

While these findings highlight potential benefits of spot melting, more research is needed to recognize possible limitations and trade-offs, which may vary with different process conditions or geometries.

From a modeling perspective, the results demonstrate the necessity of resolving mesoscopic structures at the melt pool scale, including free-surface dynamics and wetting behavior, to accurately represent the critical physical



Table 1 Properties of the Inconel 625 alloy for the simulations

Atomic number	28
Atomic mass (Da)	58.7
Liquidus temperature T_{liquidus} (K)	1623
Solidus temperature T_{solidus} (K)	1563
Density at T_{liquidus} (kg/m ³)	8000
Viscosity v (m ² /s)	0.7×10^{-6}
Surface tension σ (N/m)	$2.4470 - 3.5000 \times 10^{-4} \text{ T (K)}$
Wetting angle with substrate surface (°)	0
Wetting angle with powder particles (°)	105
Diffusivity in solid phase (m ² /s)	$2.31400 \times 10^{-6} + 2.0000 \times 10^{-9} \text{ T (K)}$
Diffusivity in liquid phase (m ² /s)	$2.43400 \times 10^{-6} + 2.0000 \times 10^{-9} \text{ T (K)}$
Isobaric volumetric heat capacity (J/m³/K)	$\begin{cases} 4.00 \times 10^{6}, & \text{if } 0\text{K} < T \le 900 \text{ K} \\ 5.50 \times 10^{6}, & \text{if } 900 \text{ K} < T \le 1563 \text{ K} \\ 6.00 \times 10^{6}, & \text{if } T > 1563 \text{ K} \end{cases}$
Latent heat of fusion (J/m ³)	2.656×10^9
Saturated vapor pressure (Antoine equation)	
$P_{sat}(T) = 10^{A-B/(C+T/K)} Pa$, where	
\mathcal{A}	11.672
\mathcal{B}	20765.0
C	0

T is the temperature in K

processes involved in defect formation during thin-wall builds.

Further study is required to assess the influence of spot melting on microstructure evolution, thermal stress development, and to explore a broader parameter space for process optimization. A comparison with alternative scanning strategies aimed at eliminating non-uniform heating would be of significant interest.

Comparison with experimental results for the current findings remains essential. This study primarily contributes to revealing the underlying physical mechanisms through numerical simulation at the melt pool scale, thereby providing a foundation for future targeted experimental and computational investigations.

Appendix

364 See Table 1.

349

350

351

352

353

354

355

356

357

358

359

360

361

362

365

366

367

368

369

370

371

372

Supplementary Information The online version contains supplementary material available at https://doi.org/10.1007/s40964-025-01377-x.

Author Contributions B.K. led the conceptualization, methodology, software development, and wrote the original draft; he also contributed to reviewing and editing the manuscript due to the revisions. M.B. contributed to validation, conceptualization, and methodology. S.B. managed the project and contributed to conceptualization and methodology. A.P. worked on visualization and software, and contributed

to conceptualization and methodology. I.I. contributed to validation, conceptualization, and methodology. A.Z. contributed to software development, methodology, and conceptualization. B.P. supervised the project and contributed to conceptualization and methodology. All authors reviewed and approved the manuscript.

374

375

376

377

378

379

380

381

382

383

384

385

386

387

388

389

390

391

392

393

394

395

396

397

398

399

Data availability No datasets were generated or analyzed during the current study.

Declarations

Conflict of interest The authors declare no conflict of interest.

References

- Yadroitsev I, Shishkovsky I, Bertrand P, Smurov I (2009) Manufacturing of fine-structured 3d porous filter elements by selective laser melting. Appl Surf Sci 255(10):5523–5527
- Su X, Yang Y, Xiao D, Luo Z (2013) An investigation into direct fabrication of fine-structured components by selective laser melting. Int J Adv Manuf Technol 64(9):1231–1238
- McGregor M, Patel S, McLachlin S, Vlasea M (2021) Architectural bone parameters and the relationship to titanium lattice design for powder bed fusion additive manufacturing. Addit Manuf 47:102273
- Lu X, Li MV, Yang H (2021) Geometric characteristics of alsi10mg ultrathin walls fabricated by selective laser melting with energy density and related process parameters. Int J Adv Manuf Technol 115(11):3773–3790
- Lu X, Yang X, Zhao X, Yang H, Li MV (2022) Additively manufactured AlSi10Mg ultrathin walls: microstructure and

 $\underline{\underline{\mathscr{D}}}$ Springer

401

402

403

404

405

406

407

408

409

410

411

412

413

414

415

416

417

418

419

420

421

422

423

424

425

426

427

428

429

430

431

432

433

434

435

436

437

438

439

440

441

442

443

- nano-mechanical properties under different energy densities and interlayer cooling times. Mater Sci Eng A 835:142652
- Brown B, Everhart W, Dinardo J (2016) Characterization of bulk to thin wall mechanical response transition in powder bed am. Rapid Prototyp J 22(5):801–809
- Wu Z, Narra SP, Rollett A (2020) Exploring the fabrication limits of thin-wall structures in a laser powder bed fusion process. Int J Adv Manuf Technol 110(1):191–207
- Korneev B, Zakirov A, Bogdanova M, Belousov S, Perepelkina A, Iskandarova I, Potapkin B (2023) A numerical study of powder wetting influence on the morphology of laser powder bed fusion manufactured thin walls. Addit Manuf 74:103705. https://doi.org/ 10.1016/j.addma.2023.103705
- Semjatov N, Wahlmann B, Körner C (2024) Multiple interaction electron beam powder bed fusion for controlling melt pool dynamics and improving surface quality. Addit Manuf 90:104316. https://doi.org/10.1016/j.addma.2024.104316
- Chakraborty A, Tangestani R, Batmaz R, Muhammad W, Plamondon P, Wessman A, Yuan L, Martin É (2022) In-process failure analysis of thin-wall structures made by laser powder bed fusion additive manufacturing. J Mater Sci Technol 98:233–243
- 11. Lee Y, Kirka MM, Raghavan N, Dehoff RR (2017) Simulation of spot melting scan strategy to predict columnar to equiaxed transition in metal additive manufacturing. In: Solid freeform fabrication 2017: proceedings of the 28th annual international solid freeform fabrication symposium—an additive manufacturing conference. University of Texas at Austin, Austin
- Nandwana P, Lee Y (2020) Influence of scan strategy on porosity and microstructure of Ti-6Al-4V fabricated by electron beam powder bed fusion. Mater Today Commun 24:100962
- Körner C (2016) Additive manufacturing of metallic components by selective electron beam melting—a review. Int Mater Rev 61(5):361–377. https://doi.org/10.1080/09506608.2016.1176289
- Galati M, Iuliano L (2018) A literature review of powder-based electron beam melting focusing on numerical simulations. Addit Manuf 19:1–20. https://doi.org/10.1016/j.addma.2017.11.001
- KiSSAM Simulation Software for Additive Manufacturing. www. kissam.cloud. Accessed May 2025
- Attar E, Körner C (2011) Lattice Boltzmann model for thermal free surface flows with liquid–solid phase transition. Int J Heat Fluid Flow 32(1):156–163. https://doi.org/10.1016/j.ijheatflui dflow.2010.09.006
- 17. Khairallah SA, Anderson AT, Rubenchik A, King WE (2016) Laser powder-bed fusion additive manufacturing: physics of

- complex melt flow and formation mechanisms of pores, spatter, and denudation zones. Acta Mater 108:36-45
- Marangoni C (1865) Sull'espansione delle Goccie D'un Liquido Galleggianti Sulla Superfice di Altro Liquido. Fratelli Fusi, Pavia
- Dantzig JA, Rappaz M (2016) Solidification: revised and expanded. EPFL Press, Lausanne
- Knight CJ (1979) Theoretical modeling of rapid surface vaporization with back pressure. AIAA J 17(5):519–523
- Klassen A (2018) Simulation of evaporation phenomena in selective electron beam melting. PhD thesis, Friedrich-Alexander-Universität Erlangen-Nürnberg
- Joy DC (1991) An introduction to Monte Carlo simulations. Scanning Microsc 5(2):4
- Murata K, Matsukawa T, Shimizu R (1971) Monte Carlo calculations on electron scattering in a solid target. Jpn J Appl Phys 10(6):678
- Govender N, Wilke DN, Kok S (2016) Blaze-DEMGPU: modular high performance dem framework for the GPU architecture. SoftwareX 5:62–66
- Gaikwad A, Imani F, Yang H, Reutzel E, Rao P (2019) In situ monitoring of thin-wall build quality in laser powder bed fusion using deep learning. Smart Sustain Manuf Syst 3(1):98–121
- Zakirov A, Belousov S, Bogdanova M, Korneev B, Iskandarova I, Perepelkina A, Potapkin B (2024) KiSSAM: efficient simulation of melt pool dynamics during PBF using GPUs. Progress in additive manufacturing, pp 1–18. https://doi.org/10.1007/s40964-023-00561-1
- Zakirov A, Belousov S, Bogdanova M, Korneev B, Stepanov A, Perepelkina A, Levchenko V, Meshkov A, Potapkin B (2020) Predictive modeling of laser and electron beam powder bed fusion additive manufacturing of metals at the mesoscale. Addit Manuf 35:101236. https://doi.org/10.1016/j.addma.2020.101236
- 28. Schwalbach EJ, Chapman MG, Groeber MA (2021) AFRL additive manufacturing modeling series: challenge 2, microscale process-to-structure data description. Integr Mater Manuf Innov 10(3):319–337

Publisher's Note Springer Nature remains neutral with regard to jurisdictional claims in published maps and institutional affiliations.

444

445

446

447

448

449

450

451

452

453

454

455

456

457

458

459

460

461

462

463

464

465

466

467

468

469

470

471

472

473

474

475

476

477

478

479

480

481

482

